

# RF-Eye: Training-free Object Shape Detection using Directional RF Antenna \*

Weiling Zheng<sup>1,2</sup>, Dian Zhang<sup>2</sup>(✉), Peng Ji<sup>2</sup>, and Tao Gu<sup>3</sup>

<sup>1</sup> RMIT University, 124 La Trobe Street, Melbourne Victoria 3000, Australia

<sup>2</sup> Shenzhen University, Nanhui Avenue 3688, Shenzhen, China

<sup>3</sup> Macquarie University, Balaclava Road, North Ryde New South Wales 2109, Australia

**Abstract.** Detecting object shape presents significant values to applications such as Virtual Reality, Augmented Reality and surveillance. Traditional solutions usually deploy camera on site and apply image processing algorithms to obtain object shape. Wearable solutions require target to wear some devices, and apply machine learning algorithms to train and recognize object behaviors. The recent advances in Radio Frequency (RF) technology offer a device-free solution to detect object shape, however a number of research challenges exist. This paper presents RF-Eye, a novel RF-based system to detect object shape without training in indoor environments. We design and implement Linear Frequency Modulated baseband signal, making it suitable for detecting object shape. We also apply the narrow pulse signal reflections and Doppler Frequency Shift to detect the full image of object shape. We implement RF-Eye on a Universal Software Radio Peripheral device. Our experimental results show that RF-Eye achieves 100% successful rate, and its performance is reliable in complicated cases.

**Keywords:** Directional Antenna · Device-free · Line-of-Sight · Radio Frequency

## 1 Introduction

Detecting object shape such as human body in a device-free manner, also known as transceiver-free, plays a significant role in applications such as Virtual Reality (VR), Augmented Reality (AR) and surveillance. One of the most common technology used for detecting objects shape is video due to its stability and simplicity [11] [12] [14] [28] [31] [40]. However, video technique usually requires suitable light condition and the line-of-sight (LoS) from camera to object. Otherwise, the object is hard to be isolated from the background. And it may therefore result in failure of detecting object shape. Moreover, vision-based solutions introduce an unavoidable problem of user privacy violation, especially in indoor environment. Radio Frequency (RF) technology would help fill this shortfall in demand. Although RF-based detection method is comparatively mature in an

---

\* This research was supported in part by NSFC 61872247.

outdoor environment. It remains challenges in indoor environment where can be complicated due to multi-path effect, i.e., wireless signals will be reflected, refracted and scattered by indoor objects. Radar and Sonar systems [9] are able to detect and capture the figure of inanimate object outdoors, e.g., planes. However, they operate at a very high frequency (i.e., millimeter or sub-millimeter wave), requiring expensive equipment which can be bulky in size. It also requires strong transmission power which it may be harmful to human health, making it almost inapplicable in indoor environments.

The lower frequency RF-based signal will most likely to be chosen in indoor environment. Most of the existing RF-based technologies in indoor can only localize and track objects. Several recent attempts [32] [41] apply machine learning algorithms to recognize human behaviors such as waving hand and falling down. However, since these solutions leverage heavily on proper training, and the training cost arises with environment or target changes. Dina Katabi et al. [1] propose to capture human figure by designing a multi-antenna Frequency Modulated Carrier Wave (FMCW) radio system. But the whole figure will be stitched together from a number of segments, i.e., sub figures, requiring multiple operations to combine partial segments to obtain the full image.

In this paper, we propose RF-Eye, an RF-based system to object shape detection in indoor environments. In our design, we face three major challenges.

First, commodity wireless signal such as WiFi is not suitable for detecting object shape due to the limitation of its narrow bandwidth (i.e.,  $20MHz$ ) [29]. Study shows that the image resolution depends much on bandwidth [29]. The most straightforward way to improve the accuracy of object shape detection is to deploy higher bandwidth wireless signal. However, indoor wireless radio usually has limited bandwidth, hence it is tricky to design a wireless radio system with bandwidth limitation. We implement Linear Frequency Modulated (LFM) baseband signal on Universal Software Radio Peripheral (USRP) device operates at  $5.8GHz$ . The instantaneous frequency of this signal is a linear function of time and the transmitted signal is a narrow pulse. As a result, both bandwidth and time-width will be improved since they are determined by frequency- and time-domain characteristics of the signal, respectively. Moreover, we leverage Quadrature Amplitude Modulation (QAM) to expand the effective bandwidth to  $120MHz$ . Therefore, it is able to capture relatively clear object shape.

Second, existing methods [1] to detect object shape usually utilize image mosaic. These approaches typically deploy multiple antennas where each antenna is responsible of capturing a partial segment, and then combine all the segments into the full image. However, the assembly process is error prone, and it often results in assembling segments in wrong positions. Our design principle is to obtain the full image one time to avoid such error. This task will become more challenging with only one antenna. In RF-Eye, we use the Doppler frequency change to achieve the full coverage of object with one antenna. Hence, it is able to capture object shape in one time.

Third, indoor environments are suffered from multi-path phenomenon, which means the signals indoors are easily reflected, refracted and scattered by indoor

objects, making the signal at the receiver is the combination of signals along multiple paths. We aim to apply one directional antenna with a narrow angle. Thus, signals from other paths not existing in the angle area are easily filtered out. It has advantages to reduce the effect of multi-path phenomenon, so as to improve the results. Based on them, we use image processing algorithms to obtain a more fine-grained object shape.

We implement RF-Eye on USRP device, and conduct extensive experiments to evaluate system performance on different objects. Our results show that RF-Eye is able to achieve 100% successful rate to detect object shape. Even for complicate object such as human body, RF-Eye is able to obtain the shape.

In summary, this paper makes the following contributions.

- We present a novel low frequency RF-based system to detect object shape in indoor environments without training.
- Our system is able to detect object shape in one go, avoiding the segment combination problem and reducing multi-path effect. We use one directional antenna instead of an antenna array to detect complex object shape based on the narrow pulse signal reflections and Doppler frequency change caused by object.
- We design Linear Frequency Modulated (LFM) baseband signal based on USRP operates at  $5.8GHz$ , which essentially leverages on QAM to expand the effective bandwidth to  $120MHz$ . We leverage image processing algorithm to improve the results. Results show that RF-Eye is able to detect contoured shapes of common indoor objects.

The rest of the paper is organized as follows. We first introduce the related work. In Section 3, we give an overview of our system design and describe the proposed algorithms. We present our implementation and experiments in Section 4. Finally, we conclude the paper and point out our future work in Section 5.

## 2 Background

In this section, we discuss various approaches of object shape detection. We divide the related work into three categories as follows.

**Camera-based Approach.** Much work [11] [12] [14] [28] [31] [40] has been done using various cameras, e.g., Multi-View cameras, Moving cameras, and Time-of-Flight cameras, and they typically utilize image processing algorithms to capture human figure. Kinect et al. [37] propose to detect human image by integrating with some infrared sensors when the light is dim. They design a  $2-D$  head contour model and a  $3-D$  head surface model. However, this approach is able to obtain coarse-grained human skeleton only. In general, camera-based approaches have a limited range of line of sight, and also they do not work in dark area. In addition, user privacy can be a big concern preventing them from being widely adopted.

**Device-based Approach.** Some existing work requires to carry a device by target. Their main purpose is to track the moving target or identify target

behaviors [25] [27] [30] [33], rather than obtain target shape. Xsens MVN [27] can track the motion of human full body using biomechanical models and sensor fusion algorithms, but it requires the target to wear inertial and magnetic sensors. The study in [30] can recognize human motion both indoors and outdoors. It also requires the target to wear ultrasonic and inertial sensors on the garment. Prakash et al. [25] measure three dimensional motion and orientation of the target, but the target has to carry RFID passive tags.

**Device-free Tracking and Behavior Identification.** Several device-free systems have been proposed to track or analyze target without the requirement of carrying any device. E-eyes [33] is able to identify human activities in a device-free manner using WiFi in indoor environments. The work in [38] proposes a software-base system to obtain high resolution power delay profiles by splicing the CSI measurements. The work in [2] [3] introduce a system called WiTrack, which tracks a user’s indoor location by using wireless signal reflections from human body, even when the user is not in line of sight. However, these systems aim for tracking user location and activities, not target shape.

**Radar and Related Systems.** Existing objection imaging systems such as radar, SAR, ISAR, X-ray, CT, MRI, B-scan [13] [19] [20] [21] [35] [36] [42] [43] use a special equipment with bulky size and high cost. For example, Radar systems [4] [6] [9] [43] are able to image the figure of inanimate object outdoors, e.g., planes. However, they operate at a very high frequency (i.e., millimeter or sub-millimeter wave), and use professional equipment which is very expensive and big in size. Furthermore, it requires strong transmission power that it may be harmful to human health, making it almost inapplicable indoors. X-ray and CT although can detect human shape indoors, it is harmful to human body [26] as well.

**Device-free Target Shape Capturing Systems.** Huang et al. [15] explore the feasibility of imaging with Wi-Fi signal by leveraging the multipath propagation method. This approach results in wireless signals light up the objects. Then, the reflection of untagged objects is used for imaging. However, due to the limitations of WiFi signal such as the narrow band property, their work can only distinguish whether there is a target or not without imaging a rough picture. Dina et al. [1] propose an approach to capture the human’s coarse skeleton figure when they stand behind a wall without wearing any device. Their system firstly collects the reflection signal from the target, then catches the different segments of human body parts. Finally, it stitches every part to form a whole image. However, the target figure cannot be figured out in one go as the entire target image is concatenated by several sub-images. How to assemble sub-images correctly remains unsolved. Tyler et al. [24] propose to image low Radar Cross Section (RCS) objects, fast moving objects in free-space and a human-shape object behind a 10cm-thick solid concrete wall with an Ultra Wide Band (UWB) Multiple-Input Multiple-Output (MIMO) phased array radar system. However, it aims to track a moving human target, not capture human shape.

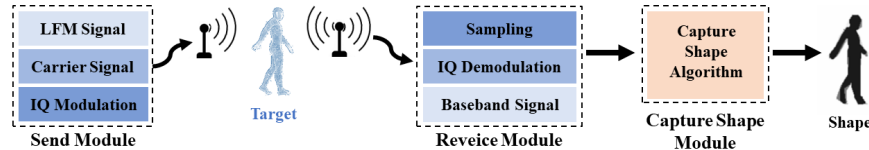


Fig. 1: Design Overview

### 3 Methodology

In this section, we first point out the challenges of capturing target shape by using RF-based technologies. We then introduce our solution to address each of the challenges. We finally present the detail algorithms to implement our ideas.

#### 3.1 Challenge

We discover two key challenges: 1) how to choose and implement radio signal, making it applicable to capture target shape in indoor environments, and 2) how to design an algorithm which is able to obtain fine-grained target shape in one go.

**Challenge 1** We first consider how to select radio signal. It is known that different radio signals have different roles [29]. Only when high frequency wavelength is comparable to the roughness of the surface, the human body becomes a scatter as opposed to a reflector [5] [8] [16]. However, it is difficult and costly to apply high frequency wave in indoor environments.

On the other hand, commodity WiFi signal is originally designed for effective data transmission by using specific modulation methods, e.g., Orthogonal Frequency Division Multiplexing (OFDM) [38] [39]. Studies show that the effectiveness of capturing target shape depends much on bandwidth [29]. Due to its narrow bandwidth of WiFi, it is hence not suitable for capturing target shape.

**Challenge 2** It is difficult to capture target shape using RF reflected signals. Although human skeleton figure can be captured in [1], their system needs to concatenate several sub-image to assemble the entire target image. We aim to design a system which is able to obtain target shape in one go without training.

#### 3.2 Our Design Principles

We now present the proposed design principles in this section.

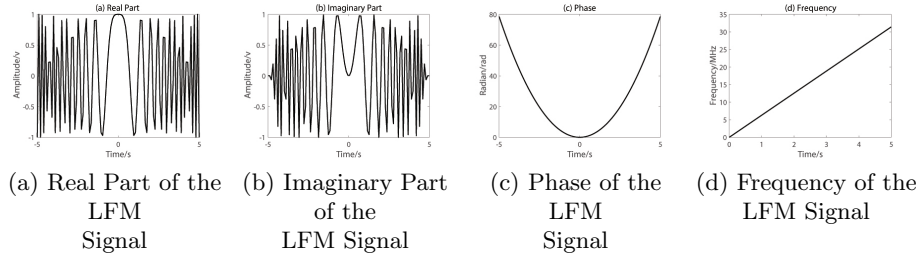


Fig. 2: LFM Signal

**Linear Frequency Modulation** According to signal and system theory [23], the product of time-width and bandwidth is a constant. The range resolution of capturing target shape depends on bandwidth  $B$ , which is  $(C/2B)$  ( $C$  is the speed of light). The bandwidth of the signal is a constant. In order to achieve both large time-width and bandwidth, we use Linear Frequency Modulation (LFM), i.e., a pulse compression method [18] [34]. In LFM, the radio frequency will increase with time. In order to expand the effective bandwidth, we also leverage Quadrature Amplitude Modulation (QAM), which is an amplitude modulation on two orthogonal carriers.

**Doppler Frequency Shift** When LFM signal is transmitted, different parts of the target will reflect the narrow pulse signal. Since target rotation/moving will cause Doppler frequency shift, such changes can be used to capture target shape. With Doppler effect, we are able to capture fine-grained target shape with different states, provided the target rotates or moves during capturing. If the target is moving, we can apply moving compensation to capture its shape. If the target is static, we may move the antenna and apply a similar approach to obtain its shape.

### 3.3 Design Overview

Figure 1 gives an overview of our system design. We first implement the LFM signal, and each LFM pulse signal contains a number of sub-pulse signals. We then leverage Quadrature Amplitude Modulation (QAM) to modulate the LFM signal. QAM is an amplitude modulation on two orthogonal carriers. The quadrature amplitude modulation signal has two carriers of the same frequency, but the phase difference is 90 degrees. One signal is called  $I$  signal, which represents in phase. Another signal is called  $Q$  signal, which represents orthogonal to  $I$  signal. When the radio signal is transmitted, it will be reflected by the target and received by the receiver. After demodulation by the receiver, we use Nyquist sampling [29] on the base frequency signal to obtain IQ data. Finally, we design our algorithm to obtain target shape.

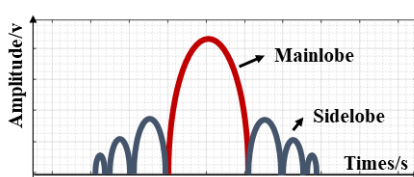


Fig. 3: Schematic of Range Sidelobes

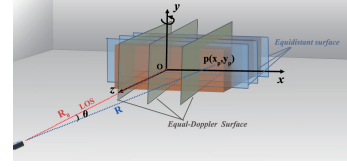


Fig. 4: Basic Idea of Capturing Target Shape

### 3.4 Linear Frequency Modulated (LFM) Signal Implementation

In Linear Frequency Modulated (LFM) signal, the instantaneous frequency is a linear function of time. The LFM signal  $S(t)$  can be represented as follows.

$$S(t) = \text{rect}\left(\frac{t}{T}\right)e^{j(2\pi f_0 t + \pi kt^2)} \quad (1)$$

where  $t$  is the time variable,  $T$  is the total time length,  $k$  is the linear frequency modulation parameter and  $f_0$  is the starting frequency, and its value is set to  $5.68GHz$ .

Figure 2 depicts the LFM signal. We can see that the real and imaginary parts of the signal function are both the oscillatory functions of time, and the oscillation frequency increases gradually as the time increases. The signal pulse phase is represented by  $\phi(t) = \pi kt^2$ , which is a quadratic function of time. The instantaneous frequency  $f$  after the time is differentiated is depicted as

$$f = \frac{1}{2\pi} \frac{d\phi(t)}{dt} = \frac{1}{2\pi} \frac{d(\pi kt^2)}{dt} \quad (2)$$

Therefore, the frequency is a linear function of time  $t$ , the slope is  $k$ , as shown in Figure 2(d).

### 3.5 Reduce the effect of sidelobe

The presence of the sidelobes, as shown in Figure 3 will obscure the resolution of the neighboring target, resulting in decreasing the signal detection capability and increasing false alarm.

When the desired narrow pulse is obtained by LFM, which is one of the pulse compression methods, the received pulse strength will decrease significantly due to strong clutter, noise and other factors. A series of range sidelobes, whose amplitude is lower than narrow pulse, often appear on both sides of the mainlobe [17] as a result of these factors. The presence of range sidelobes will obscure the resolution of the neighboring target, and reduce the signal detection capability of small target. The false alarm rate will be high without suppressing sidelobes disturbance. A matched filter based on weighted processing, i.e., a window technique, can be used to suppress high range sidelobes. Window techniques

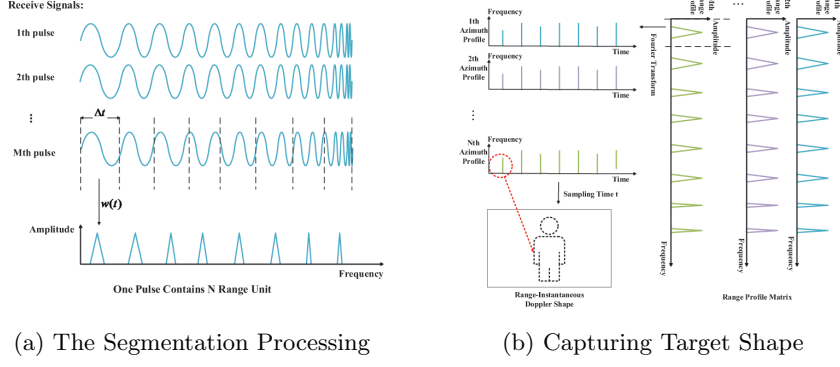


Fig. 5: Illustration of Algorithm

can reduce the spectral leakage when the digital signal is processed for discrete spectrum analysis.

Both the Hamming Window and the Hanning Window are improved ascending cosine window but with different Weighting Coefficient. The Hamming Window has a better inhibition of spectral leakage than the Hanning Window [17]. Therefore, we utilize the Hamming Window to suppress high range sidelobes.

The time domain of the Hamming Window function can be expressed as follows.

$$w(k_h) = 0.54 - 0.46 \cos\left(\frac{2\pi k_h}{N-1}\right) \quad k_h = 1, 2, \dots, N \quad (3)$$

where  $N$  is the length of the window.

### 3.6 Modulation and Demodulation

In the design of signal modulation and demodulation, we leverage Quadrature Amplitude Modulation (QAM) to modulate LFM signal. QAM is an amplitude modulation on two orthogonal carriers of the same frequency, but the phase difference is 90 degrees (quarter cycle, from the integral term). One signal is called  $I$  signal, which represents in phase. Another signal is called  $Q$  signal, which represents orthogonal to  $I$  signal. From a mathematical point of view, these two signals can be expressed as a sine function and a cosine function, respectively. Therefore, Equation 1 can also be expressed as follows.

$$\begin{aligned} I(t) &= \cos(2\pi f_0 t + \pi kt^2) \operatorname{rect}\left(\frac{t}{T}\right) \\ Q(t) &= \sin(2\pi f_0 t + \pi kt^2) \operatorname{rect}\left(\frac{t}{T}\right) \end{aligned} \quad (4)$$

Figure 6 illustrates the procedure for both modulation and demodulation. The two orthogonal signals are obtained from after the LFM signals multiply by in-phase signal and quadrature signal of the carrier signal, respectively. They are

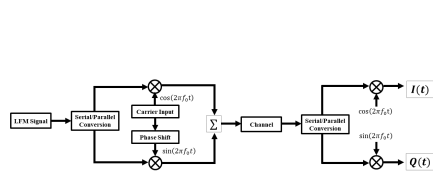


Fig. 6: Schematic of IQ modulation and Demodulation



Fig. 7: Illustration of Our Experiments

stacked as modulated signal at the time of transmission. After reflecting from the target, the time-domain sampling signals will be obtained by quadrature demodulation to received signal, and recorded as digital data.

In detail, in the modulation step, the signal  $S_b(t) = I(t) + jQ(t)$  is modulated on the frequency carrier.  $I$  signal is multiplied by  $\cos(2\pi f_0 t)$ , while  $Q$  signal is multiplied by  $\sin(2\pi f_0 t)$ . The output signal is then

$$\begin{aligned} S_c(t) &= I(t)\cos(2\pi f_0 t) - Q(t)\sin(2\pi f_0 t) \\ &= I(t)\cos(\omega_0 t) - Q(t)\sin(\omega_0 t) \end{aligned} \quad (5)$$

When the receiver receives  $S_c(t) = I(t) + jQ(t)$ , the  $I$  signal can be obtained by multiplying  $\cos(2\pi\omega_0 t)$ . Then the  $I$  signal can be calculated by the integral result as follows.

$$\begin{aligned} &\frac{2}{T} \int_{-\frac{T}{2}}^{\frac{T}{2}} [I(t)\cos(\omega_0 t) - Q(t)\sin(\omega_0 t)\cos(\omega_0 t)]dt \\ &= \frac{2}{T} \int_{-\frac{T}{2}}^{\frac{T}{2}} I(t)\cos^2(\omega_0 t) - Q(t)\sin(\omega_0 t)\cos(\omega_0 t)dt \\ &= \frac{2}{T} \cdot \frac{I(t)}{2} \cdot T \\ &= I(t) \end{aligned} \quad (6)$$

The other  $Q$  signal can be calculated similarly.

### 3.7 Algorithm to Capture Target Shape

In this subsection, we present our algorithm to capture target shape.

Based on the radio implementation, the transmitted signal is a narrow pulse. A certain part of the target object will reflect or scatter the narrow pulse signal. We refer such point as the target reflection (scattering) point. If the target rotates, it will produce a micro-Doppler shift. Accordingly, for one reflected (scattered) narrow pulse signal received by the receiver, we may form one point

of the target shape. Since there are a large number of such reflected (scattered) narrow pulse signals, we can eventually obtain the entire target shape.

As shown in Figure 4, the point  $T$  is the transmitter. Along the Line-of-Sight (LOS) path from the transmitter to the target two-dimensional plane, the intersection point on the plane is the center of the coordinates, which is  $(x_0, y_0)$ . The LOS distance is  $R_0$ . Suppose that the target will rotate along the  $y$  axis (can be easily extended to other direction), the surface parallel to the plane formed by the  $y$  axis and the  $z$  axis is called Equal-Doppler Surface (parallel to the LOS), since each surface will cause same Doppler frequency change for the signals. Also, the surface parallel to the plane formed by the  $x$  axis and the  $y$  axis is called Equidistant Surface (vertical to the LOS).

For a certain reflection (scattering) point  $P(x_p, y_p)$  on the target, the distance  $R$  from transceiver to this point can be represented below.

$$R \cong R_0 + x_0 \sin \omega t + y_0 \cos \omega t \quad (7)$$

The Doppler Frequency  $f_d$  is calculated as

$$f_d = \frac{2\nu}{\lambda} = \frac{2dr}{\lambda dt} = \frac{2x\omega}{\lambda} \cos \omega t - \frac{2y\omega}{\lambda} \sin \omega t \quad (8)$$

According to Equations 7 and 8, when either  $t$  or the rotation angle  $\Delta\varphi = \omega t$  is very small, we can do the following linear approximation.

$$R \cong R_0 + y f_d = \frac{2x\omega}{\lambda} \quad (9)$$

From the above equation, suppose  $\Delta x$  is the required Azimuth resolution (target capturing accuracy), we can conclude that the Doppler resolution should reach

$$\Delta f_d = \frac{2\omega}{\lambda} \Delta x \quad (10)$$

The real Doppler resolution determined by coherent processing time  $\Delta f_d = \frac{1}{T}$ , combining Equation 10, we have real Azimuth resolution  $\rho_0$  as

$$\rho_0 = \frac{\lambda}{2\omega T} = \frac{\lambda}{2\Delta\varphi} = \Delta x \quad (11)$$

$\Delta\varphi$  is the rotation angles within the coherent processing time  $T$ , wavelength  $\lambda$  is determined by the carrier frequency. From this Azimuth resolution is directly proportional to carrier frequency and rotation angles  $\Delta\varphi$ . Azimuth resolution improved with the coherent accumulative rotation angles increases within the limit in the range-doppler imaging method. Excessive rotation angles  $\Delta\varphi$  may cause a blurring effect to the image of target shape since the reflection (scattering) point which has long distance to the reference rotation center moves over a resolution unit.

The signals to a discrete Doppler domain by Fourier transform. Thus, we can obtain the one-dimensional Doppler spectrum of the target. When the wavelength is fixed, the Doppler frequency change caused by the different position  $i$  of target can be used to achieve the ranging profile of signals at position  $i$ .

Our algorithm of capturing target shape is based on Short-time Fourier Transform [23]. It can use the time-frequency joint function to describe the density and intensity of the signal at each time and frequency point. The detail is listed as follows.

We therefore use the time-domain analysis method in the shape capturing process since range-Doppler shape can be obtained by analysing the frequency component of the giving signal at various time based on time-frequency transform without compensating for complex translational components. Our algorithm of capturing target shape is based on Short-time Fourier Transform [23]. We use the time-frequency joint function to describe the density and intensity of the signal at each time and frequency point. The detail is described as follows.

Suppose we capture the target shape into two-dimensions, and in a time period  $P$  in total we have received  $M$  number of reflected (scattered) narrow pulse signals. For each signal  $i$ , there are  $N$  number of sub pulse signals. We divide the time period  $P$  into several shorter series, whose time length is  $\Delta t$ . Then we use the Fourier transform method to describe the frequency component of the signal. This segmentation is achieved by multiplying the sliding window  $w(t)$  and the signal  $s(t)$ , which can be represented as follows.

$$S(t, \omega) = \int_{-\infty}^{+\infty} s(\tau)w(\tau - t)e^{-j\omega\tau} dt \quad (12)$$

During each sampling period  $\Delta t$ , The time-frequency distribution of different pulse are combined together. Thus, we can obtain the instantaneous ranging profile of each reflection (scattering) point. As shown in Figure 5, in total, we have  $M$  number of ranging profiles corresponding to  $M$  number of reflected (scattered) narrow pulse signals. For each ranging profile in each sampling period  $\Delta t$ , there are  $N$  number of ranging units (Azimuth Profiles) corresponding to  $N$  sub-pulse signals. Then the azimuth Doppler analysis of each ranging profile is carried out, we may get the two-dimensional image of the target.

Through the above solution, the two-dimensional ranging-Doppler image is transformed into a three-dimensional time-ranging-Doppler stereogram. Then we take the sample time into account, you can get a ranging-Doppler image along the time series. Thus, in each of the individual time sample, we may provides a high-resolution image. Then we sort the reflection (scattering) signal according to its ranging profile, time-frequency distribution of signal  $s$  is  $s(t)$ .

Then we combine all the Doppler spectra of the signals at one time, to achieve the target shape.

In coherent processing time, the object has a center of rotation, then the reflection (scattering) signal is received in the range unit  $z$  could be expressed as follows:

$$S_R(t)|_z = \sum_{k=1}^{N_k} A_k e^{-j4\pi(Bw(n-1)/N + f_0)r(t)/c} \quad (13)$$

where  $N_k$  is the number of reflection (scattering) points of this range unit,  $A_k$  is the amplitude of the  $K$ th reflection (scattering) point  $(x_k, y_k)$  on the target.

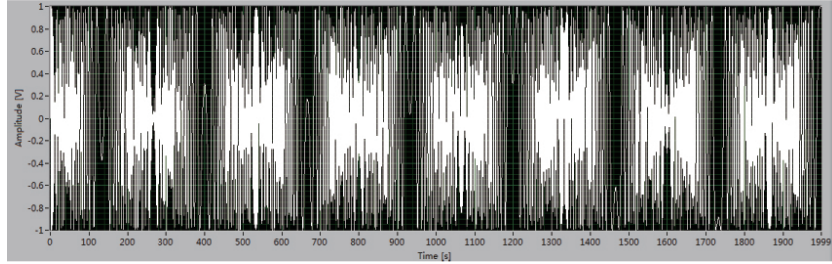


Fig. 8: Implementation Result of LFM Signal

As Figure 5 depicted, the reflection (scattering) signal can be divided into a range of short time series, then its frequency components can be described by using Fourier Transform. The segmentation processing is implemented by multiplying a sliding window  $w(t)$  and signal. On one hand, the length of the window function determines the resolution of time-domain frequency; on the other hand, the shape of the window function determines the sidelobe level and the resolution of frequency-domain. Here, the Hamming window is more adaptable to a further experiment [17] [29].

According to Equation 10, the Doppler of reflection (scattering) wave is independent of temporal variations, hence we can get time-domain distribution of current range unit signal by performing the following windowed fourier transform, combining Equation 12.

$$S(t, \omega) = \int_{-\infty}^{+\infty} s_R(\tau)w(\tau-t)e^{-j\omega\tau} dt \quad (14)$$

For moment  $t$ , the STFT to the signal  $S_R(t)|_z$  is tantamount to Fourier Transform to the value of signal multiply by moment  $t$ -centred Window Function  $w(\tau-t)$ . Because of the signal at this window segment can be approximated as steady and time-invariant. The time-frequency distribution of the signal could be obtained using Equation 13. There are considerable time-frequency distribution of pulse at the same moment. We will get the instantaneous range profile of each reflection (scattering) signal at different moment if we grouping these time-frequency distribution. In the final step, Doppler analysis of the instantaneous range profile uses Fourier Transform along the range unit can display the two-dimensional shape of the target object.

### 3.8 Operator Selection to Detect Image Edge

According to previous approach, we may get the target's RF shape. The capturing image of target object has a relatively clear center and a hazy outer edge. Using edge detection operators can adaptively estimate the edge points of target shape so as to extract and clarify the edge. The operator we have chosen is Prewitt Operator [22].

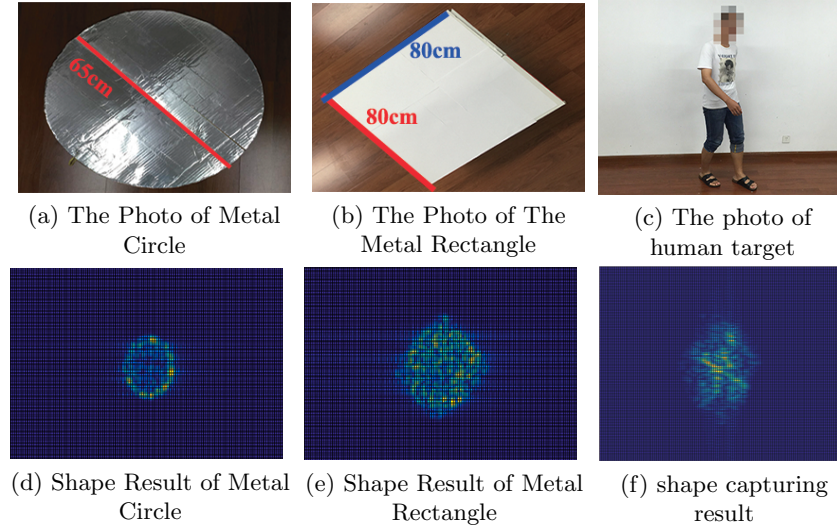


Fig. 9: RF-Eye Result of different Target Shape

Mathematically, the operator uses two kernels, which are convolved with the original image, to calculate approximations of the derivatives. Suppose  $I_a$  is the source image.  $G_x$  and  $G_y$  contain horizontal and vertical derivative approximations of  $I_a$ , respectively.

$$G_x = \begin{bmatrix} -1 & 0 & +1 \\ -1 & 0 & +1 \\ -1 & 0 & +1 \end{bmatrix} * I_a G_y = \begin{bmatrix} -1 & -1 & -1 \\ 0 & 0 & 0 \\ +1 & +1 & +1 \end{bmatrix} * I_a \quad (15)$$

At each point in the image, the resulting gradient approximations can be combined to give the gradient magnitude, using

$$G = \sqrt{G_x^2 + G_y^2} \quad (16)$$

Therefore, edge detection of the target can be realized.

## 4 Evaluation

We now move to implement and evaluate RF-Eye. In this section, we first introduce our experimental setup and the LFM radio implementation. We present the result of LFM signal and also the result of capturing different target shapes. Finally, we discuss the impact of key factors affecting system performance.

### 4.1 Experiment Setup and Radio Implementation

Our prototype system consists of two components: hardware and software components.

**Hardware Component:** We implement our system on a USRP (Universal Software Radio Peripheral) platform with a directional antennas. *NI USRP-2953R* software radio generates a  $5.8GHz$  modulated signal with the maximum bandwidth of  $120MHz$ . The transmission power is set to  $30mW$ . In our experiments, we use only one off-the-shelf parabolic antenna. The antenna has a  $32dbi$  gain and  $6^\circ$  horizontal beam width and vertical beam width. Our RF-Eye system generates a frequency chip which repeatedly sweep the band  $5.68 \sim 5.8GHz$ .

**Software Component:** We implement the signal processing algorithm in MATLAB on a commercial Lenovo desktop computer with a  $3.3Ghz$  Intel *i5* processor and  $16GB$  of RAM.

**Radio Implementation:** We implement the LFM signal based on the USRP platform. Figure 8 shows our implementation results. The  $x$  axis in the figure is the time domain, and the  $y$  axis is the amplitude of the signal. We observe that the frequency increases with time.

#### 4.2 Result of Capturing Target Shape

In this section, we show the result of our first experiment to capture the target shape, concerning both regular and complex target shapes.

In total, we perform 20 rounds of different target tests, including different targets with different shapes. Figure 9(a) shows one original shape of the test target: a mental circle with a diameter of  $65cm$ . Figure 9(b) shows another original shape of test target: a mental rectangle with a side length of  $80cm$ . Figure 9(d) and Figure 9(e) show the RF-Eye results, respectively. We observe that our system perform accurately to identify the shapes.

Next, we perform an experiment with complex shape. Human body is widely regarded as an irregular object with complex geometry shape, and Figure 9(c) shows the result of a human target. From the image result shown in Figure 9(f), we see that RF-Eye is able to identify the complete human image successfully. The imaging result clearly present the complete human shape with clear body parts, e.g., the head, arms and legs. We may even observe the gesture from the imaging obtained.

In summary, our RF-Eye system is able to successfully recognize target shape, even its shape is complex.

#### 4.3 The Impact of Sampled Signal Pulse Number

The number of pulse signals  $M$  is a key parameter in our algorithm to decide the target shape resolution. If this value is set too low, the accuracy will be affected. If this value is set too high, the latency will increase.

Therefore, for each target shape, we test the signal sample numbers from 1000 to 15000, to obtain the capturing result. Figure 10(a) ~ Figure 10(f) shows the imaging results of the circle with different sampled signal pulse number, respectively. We can observe, when the sampled number increases, the edge is more clear. Similarly, Figure 11(a) ~ Figure 11(f) shows the imaging results of

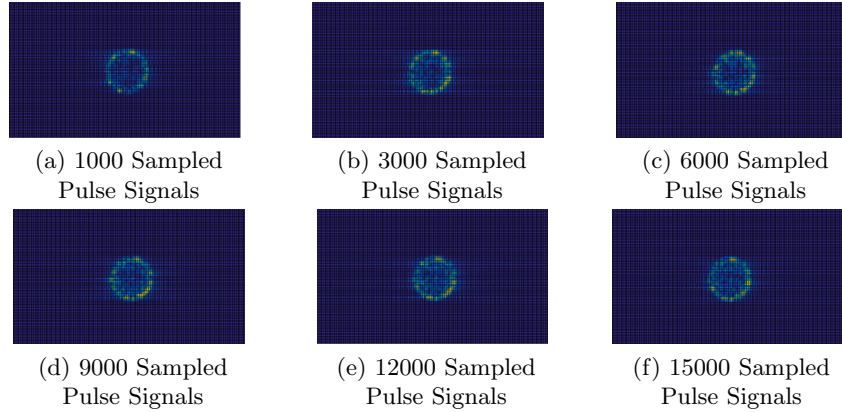


Fig. 10: Impact of Sampled Pulse Signal Number on Circular Target

the rectangle with different sampled signal pulse number, respectively. We can see that, the rectangle result is more influenced by sampled signal pulse number since it is harder to get a very clear edge at the corner of the rectangle compared to other parts. The reason may be due to that less reflected signals by the sharp corner will enter the acceptable range of the directional antenna.

For more complex human target, we increase the sample range accordingly. The sampled signal pulse number varies from 1000 to 30000. Figure 12(a) ~ Figure 12(e) show the imaging results of the human target with 1000, 5000, 10000, and 30000 signal sample numbers, respectively. We can see that, as the sampled signal pulse number increase, the body part becomes more clearly, especially for the limbs. When the sampled number is 1000 as shown in Figure 12(a), we may roughly recognize it is a human, but limb parts are blurry. When the sampled number increases to 30000 as shown in Figure 12(d), we are able to see the head, arms and legs very clearly.

#### 4.4 Impact of Window Functions

In this section, we investigate how window functions will influence the experiment results. Choosing an appropriate window function may reduce the size of the side lobe of leakage and improve the frequency resolution capability, resulting in more clear images.

In order to investigate how the window functions will influence the results, we perform several experiments based on the imaging result of human target, utilizing four typical window functions, Kaiser Window, Hanning Window, Hamming Window and Blackman Window. Figure 13 shows the imaging results after processing by these four windows, respectively. We observe that, actually there are no big difference for the results. Therefore, in our experiment, we utilize Hamming Window by default.

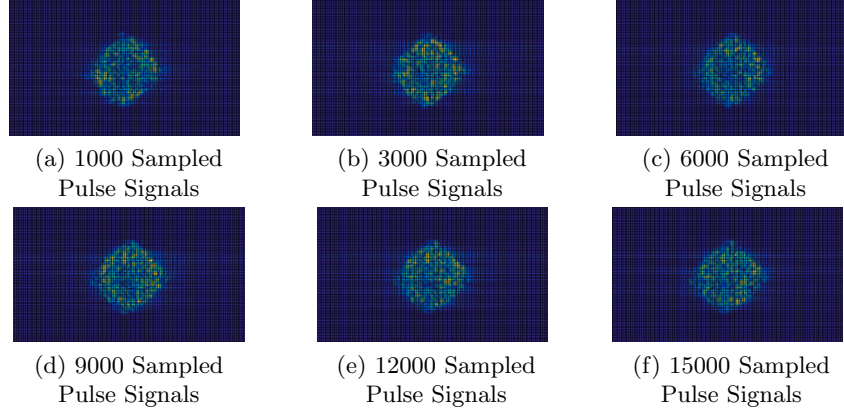


Fig. 11: Impact of Sampled Pulse Signal Number on Rectangular Target

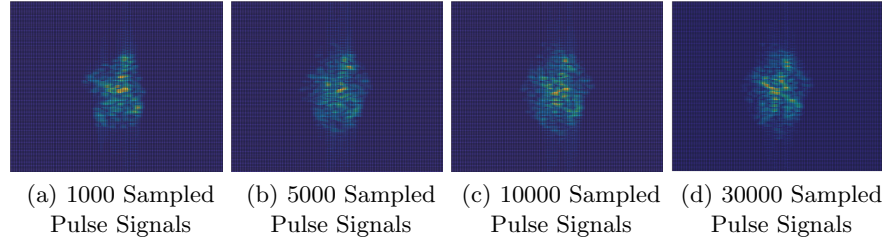


Fig. 12: Impact of Sampled Pulse Signal Number on Human Target

#### 4.5 Edge Detection Algorithm Comparison

To capture the image of a target shape in one go, we perform the Prewitt algorithm to highlight the edge of the shape and obtain a clearer contour shape of the target. In this section, we compare our algorithm with others such as Roberts and Sobel algorithm [7] [10]. Figure 14 and Figure 15 show the circle and rectangle results before and after using image processing algorithms, respectively. It is obvious to see that, when leveraging Prewitt and Sobel Operator, the contour shape presents the clearest image. The Roberts Operator does not work as good as Sobel and Prewitt. And Prewitt operator is a little bit better. Therefore, we choose Prewitt operator by default to obtain the shape edge of the RF-Eye image.

#### 4.6 Latency

The latency of RF-Eye depends on the time of both signal sampling acquisition and target shape capturing. The time cost of the signal sampling acquisition can be negligible since RF-Eye captures millions of sampling data within 1ms through the USRP based system. The time cost of the second part depends

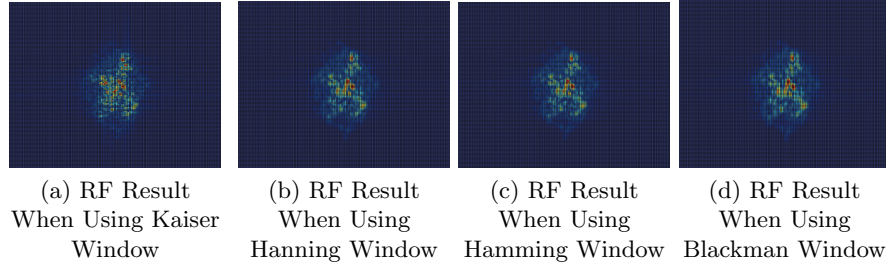


Fig. 13: Comparison of Different Window Function

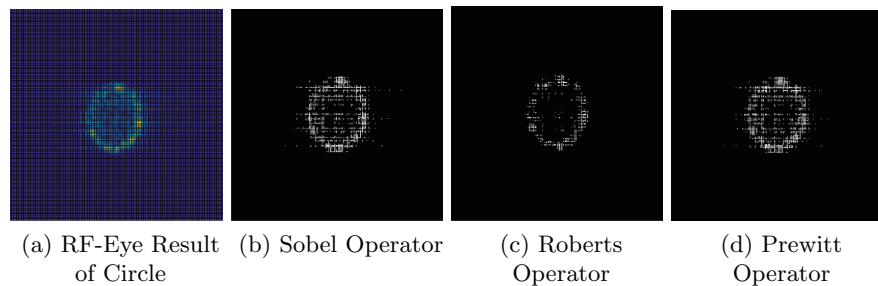


Fig. 14: Comparison of Different Edge Operator (circle)

on the number of sampling data and the performance of the system. Figure 16 shows the latency of RF-Eye. As shown in the figure, based on the hardware we introduced before in the experimental setup section, the latency of RF-Eye is about  $23s$  when the number of sampling data is 1000. The latency of RF-Eye is about  $237s$  while the number of sampling data is 10000. The latency surely will decrease if we use a high-performance computer or reduce the number of sampling data.

In order to get a clear trade-off between accuracy and latency, in real-world scenarios, users may choose preferred number of sampling data to achieve their desired results.

## 5 Discussion

In this section, we review several critical decisions in our current design, and also discuss the limitations of our system.

### 5.1 How to Choose Carrier Frequency

Actually, RF-Eye is adaptive to other carrier frequency like the  $2.4GHz$ . In such scenario, the bandwidth also can be expanded far greater than  $20MHz$ . The current upper bound is  $120MHz$ , which is limited by the USRP hardware

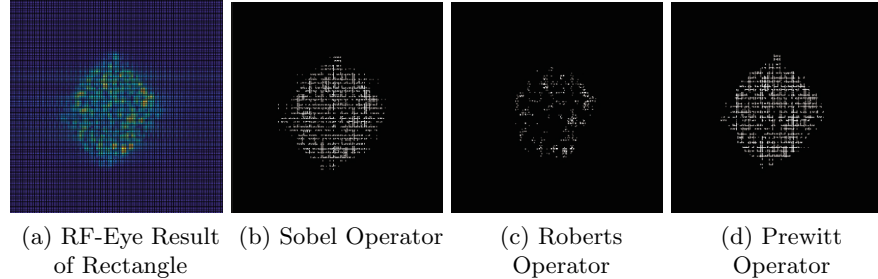


Fig. 15: Comparison of Different Edge Operator (rectangle)

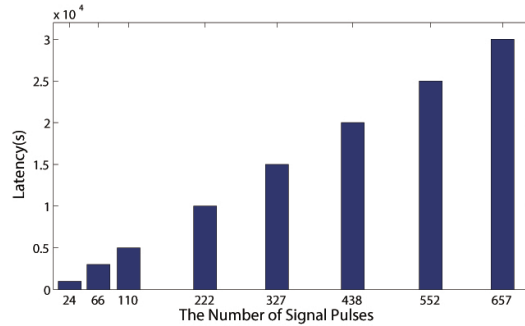


Fig. 16: The latency of RF-Eye

features. It can be further expanded using other hardware. Why in this work we choose the carrier frequency as  $5.8GHz$ , is due to the following reason. Compare to the wavelength  $11.6cm$  of  $2.4GHz$ , the wavelength of  $5.8GHz$  is  $4.8cm$ , making it not so easier to diffract small size targets or the small parts of the target, e.g., the human hand or limb. The signal can be reflected effectively and we can get the shape results more accurately. If users aim to capture the target with larger size, they may choose  $2.4GHz$  to apply our approach similarly.

## 5.2 Antenna Rotation

RF-Eye uses the narrow pulse signal reflections and Doppler frequency change caused by the rotate target to get the target shape. The limitation is the target will rotate in the real scenario. In reality, there are many possible ways to overcome such limitation. For example, if moving compensation are considered, our system is easily to be extend to moving target. Even for the static target, we may choose to move the antenna instead and apply the same approach. But this work is our first try, it can be further investigated in our future work.

## 6 Conclusion & Future Work

This paper presents RF-Eye, an RF-based system to capture complete target shape in indoor environments without training. Different from existing systems, RF-Eye exploits the basic characteristics of electromagnetic waves and implements a customized radio to efficiently capture complete target shape in one go. We use the narrow pulse signal reflections and Doppler frequency shift by the target to get the target image, and utilize image processing approach to obtain the shape of the target. Our experimental results show that RF-Eye successfully recognizes target shape (i.e., the successful recognition ratio reaches 100%). We also demonstrate that even for complicate targets our system is able to recognize and obtain its shape.

In our future work, we will investigate the impact of the bandwidth on the shape result. Second, we may change to other carrier frequency. At last, we will perform experiment to capture the shape of static target, we can move the antenna instead by applying the similar approach.

## References

1. Fadel Adib, Chen Yu Hsu, Hongzi Mao, Dina Katabi, and Fr Durand. Capturing the human figure through a wall. *Acm Transactions on Graphics*, 34(6):1–13, 2017.
2. Fadel Adib, Zachary Kabelac, and Dina Katabi. Multi-person localization via rf body reflections. In *Usenix Conference on Networked Systems Design and Implementation*, pages 279–292, 2015.
3. Fadel Adib, Zachary Kabelac, Dina Katabi, and Robert C Miller. 3d tracking via body radio reflections. pages 317–329, 2014.
4. Roger Appleby and Rupert N. Anderton. Millimeter-wave and submillimeter-wave imaging for security and surveillance. *Proceedings of the IEEE*, 95(8):1683–1690, 2007.
5. M. A Biot. Some new aspects of the reflection of electromagnetic waves on a rough surface. *Journal of Applied Physics*, 28(12):1455–1463, 1957.
6. Ken B. Cooper, Robert J. Dengler, Nuria Llombart, Tomas Bryllert, Goutam Chattopadhyay, Erich Schlecht, John Gill, Choonsup Lee, Anders Skalare, and Imran Mehdi. Penetrating 3-d imaging at 4- and 25-m range using a submillimeter-wave radar. *IEEE Transactions on Microwave Theory & Techniques*, 56(12):2771–2778, 2008.
7. Davis D. A real-time regenerative response method of equalizing a sound system. In *Journal of the Audio Engineering Society*, volume 23, pages 300–2, May 1975.
8. H. Davies. The reflection of electromagnetic waves from a rough surface. *Proceedings of the IEE - Part III: Radio and Communication Engineering*, 101(70):118, 2010.
9. R. J. Dengler, K. B. Cooper, G. Chattopadhyay, I. Mehdi, E. Schlecht, A. Skalare, C. Chen, and P. H. Siegel. 600 ghz imaging radar with 2 cm range resolution. In *Microwave Symposium, 2007. IEEE/MTT-S International*, pages 1371–1374, 2007.
10. H. Farid and E.P. Simoncelli. Optimally rotation-equivariant directional derivative kernels. In *InInternational Conference on Computer Analysis of Images and Patterns*, volume 1296, page 207–214. Springer, 1997.

11. J. Gall, C. Stoll, E. De Aguiar, C. Theobalt, B. Rosenhahn, and H. P. Seidel. Motion capture using joint skeleton tracking and surface estimation. pages 1746–1753, 2009.
12. Varun Ganapathi, Christian Plagemann, Daphne Koller, and Sebastian Thrun. Real time motion capture using a single time-of-flight camera. In *Computer Vision and Pattern Recognition*, pages 755–762, 2010.
13. D. E. Goertz, E Cherin, A Needles, R Karshafian, A. S. Brown, P. N. Burns, and F. S. Foster. High frequency nonlinear b-scan imaging of microbubble contrast agents. *IEEE Transactions on Ultrasonics Ferroelectrics & Frequency Control*, 52(1):65–79, 2005.
14. N Hasler, B Rosenhahn, T Thormahlen, and M Wand. Markerless motion capture with unsynchronized moving cameras. In *Computer Vision and Pattern Recognition, 2009. CVPR 2009. IEEE Conference on*, pages 224–231, 2009.
15. Donny Huang, Rajalakshmi Nandakumar, and Shyamnath Gollakota. Feasibility and limits of wi-fi imaging. In *Proceedings of the 12th ACM Conference on Embedded Network Sensor Systems*, pages 266–279, 2014.
16. M Katzin. *The scattering of electromagnetic waves from rough surfaces*. Pergamon Press,, 1963.
17. John Daniel Kraus and Ronald J Marhefka. Antennas for all applications. *Mcgraw*, -1, 2002.
18. Q. I. Lin, Tao Ran, Siyong Zhou, and Wang Yue. Detection and parameter estimation of multicomponent lfm signal based on the fractional fourier transform. *Science in China*, 47(2):184–198, 2004.
19. M Lustig and Jm Donoho, Dpauly. Sparse mri: The application of compressed sensing for rapid mr imaging. *Magnetic Resonance in Medicine*, 58(6):1182–C1195, 2007.
20. Randolph L Moses, Lee C Potter, Hung Chih Chiang, Michael A Koets, and Ashutosh Sabharwal. A parametric attributed scattering center model for sar automatic target recognition. *Proceedings of the Image Understanding Workshop*, pages 849–860, 1998.
21. P Mozzo, C Procacci, A Tacconi, P. T. Martini, and I. A. Andreis. A new volumetric ct machine for dental imaging based on the cone-beam technique: preliminary results. *European Radiology*, 8(9):1558, 1998.
22. J Prewitt. Object enhancement and extraction. In *Object enhancement and extraction. Picture processing and Psychopictorics*, volume 10, pages 15–19, 1970.
23. J. G. Proakis and M. Salehi. Digital communications. *Digital Communications*, 73(11):3–5, 2015.
24. Tyler S. Ralston, Gregory L. Charvat, and John E. Peabody. Real-time through-wall imaging using an ultrawideband multiple-input multiple-output (mimo) phased array radar system. In *IEEE International Symposium on Phased Array Systems and Technology*, pages 551–558, 2010.
25. Ramesh Raskar, Hideaki Nii, Bert Dedecker, Yuki Hashimoto, Jay Summet, Dylan Moore, Yong Zhao, Jonathan Westhues, Paul Dietz, and John Barnwell. Prakash:lighting aware motion capture using photosensing markers and multiplexed illuminators. *Acm Transactions on Graphics*, 26(3):36, 2007.
26. S Ratnapalan, Y Bentur, and G Koren. "doctor, will that x-ray harm my unborn child?". *CMAJ : Canadian Medical Association journal = journal de l'Association medicale canadienne*, 179(12):1293, 2008.
27. Daniel Roetenberg, Henk Luinge, and Per Slycke. Xsens mvn: Full 6dof human motion tracking using miniature inertial sensors. *Xsens Motion Technologies Bv*, 2009.

28. Jamie Shotton, Alex Kipman, Alex Kipman, Mark Finocchio, Mark Finocchio, Andrew Blake, Richard Moore, and Richard Moore. Real-time human pose recognition in parts from single depth images. *Communications of the ACM*, 56(1):116–124, 2013.
29. David Tse and Pramod Viswanath. Fundamentals of wireless communications 12. 3(5):B6–1 – B6–5, 2005.
30. Daniel Vlasic, Rolf Adelsberger, Giovanni Vannucci, John Barnwell, Markus Gross, and Wojciech Matusik. Practical motion capture in everyday surroundings. In *Acm Siggraph*, page 35, 2007.
31. Daniel Vlasic, Ilya Baran, and Wojciech Matusik. Articulated mesh animation from multi-view silhouettes. *Acm Transactions on Graphics*, 27(3):1–9, 2008.
32. Guanhua Wang, Yongpan Zou, Zimu Zhou, Kaishun Wu, and Lionel M. Ni. We can hear you with wi-fi! In *Proceedings of the 20th Annual International Conference on Mobile Computing and Networking*, MobiCom ’14, pages 593–604, New York, NY, USA, 2014. ACM.
33. Yan Wang, Jian Liu, Yingying Chen, Marco Gruteser, Jie Yang, and Hongbo Liu. E-eyes: device-free location-oriented activity identification using fine-grained wifi signatures. In *International Conference on Mobile Computing and NETWORKING*, pages 617–628, 2014.
34. Yong Wang and Yi Cheng Jiang. Detection and parameter estimation of multicomponent lfm signal based on the cubic phase function. *Eurasip Journal on Advances in Signal Processing*, 2008(1):743985, 2008.
35. D. A. White, C. Jones, and W. Forman. An investigation of cooling flows and general cluster properties from an x-ray image deprojection analysis of 207 clusters of galaxies. *Monthly Notices of the Royal Astronomical Society*, 292(2):419, 1997.
36. Ruth M Woodward, Bryan E Cole, Vincent P Wallace, Richard J Pye, Donald D Arnone, Edmund H Linfield, and Michael Pepper. Terahertz pulse imaging in reflection geometry of human skin cancer and skin tissue. *Physics in Medicine & Biology*, 47(21):3853–3863, 2002.
37. L. Xia, C. C. Chen, and J. K. Aggarwal. Human detection using depth information by kinect. In *CVPR 2011 WORKSHOPS*, pages 15–22, June 2011.
38. Yaxiong Xie, Zhenjiang Li, and Mo Li. Precise power delay profiling with commodity wifi. In *International Conference on Mobile Computing and NETWORKING*, pages 53–64, 2015.
39. Yaxiong Xie, Zhenjiang Li, Mo Li, and Kyle Jamieson. Augmenting wide-band 802.11 transmissions via unequal packet bit protection. In *IEEE INFOCOM 2016 - the IEEE International Conference on Computer Communications*, pages 1–9, 2016.
40. M. Ye, H. Wang, N. Deng, X. Yang, and R. Yang. Real-time human pose and shape estimation for virtual try-on using a single commodity depth camera. *IEEE Transactions on Visualization & Computer Graphics*, 20(4):550–9, 2014.
41. Kaishun Wu Yuxi Wang and Lionel M. Ni. Wifall: Device-free fall detection by wireless networks. *IEEE Transactions on Mobile Computing*, 16(2):581–594, 2017.
42. Lei Zhang, Mengdao Xing, Cheng Wei Qiu, Jun Li, and Zheng Bao. Achieving higher resolution isar imaging with limited pulses via compressed sampling. *IEEE Geoscience & Remote Sensing Letters*, 6(3):567–571, 2009.
43. Yanzi Zhu, Yibo Zhu, Ben Y. Zhao, and Haitao Zheng. Reusing 60ghz radios for mobile radar imaging. In *International Conference on Mobile Computing and NETWORKING*, pages 103–116, 2015.